Dysregulated intestinal nutrient absorption in obesity is associated with epigenomic alterations in epithelia

Dilhana S. Badurdeen[1], Zhen Li[1], Jeong-Heon Lee[2], Tao Ma[3], Aditya Vijay Bhagwate[3], Rachel Latanich[4], Arjit Dogiparthi[4], Tamas Ordog[5], Olga Kovbasnjuk[6], Vivek Kumbhari[1], Jennifer Foulke-Abel[4]*

[1]Division of Gastroenterology and Hepatology, Mayo Clinic Florida, Jacksonville, FL 32224, USA

[2]Division of Experimental Pathology and Laboratory Medicine, Department of Laboratory Medicine, and Pathology, and Center for Cell Signaling in Gastroenterology (C-SiG), Mayo Clinic, Rochester, MN 55905, USA

[3]Department of Quantitative Health Sciences, Mayo Clinic, Rochester, MN 55905, USA

[4]Division of Gastroenterology and Hepatology, Johns Hopkins University School of Medicine, Baltimore, MD 21205, USA

[5]Department of Physiology and Biomedical Engineering, and Division of Gastroenterology and Hepatology, Department of Medicine, Mayo Clinic, Rochester, MN 55905, USA

[6]National Institute for General Medical Sciences, Bethesda, MD 20892, USA

RUNNING HEAD: Dysregulated intestinal absorption phenotype in obesity

* **CORRESPONDING AUTHOR:** Jennifer Foulke-Abel, PhD, Johns Hopkins University School of Medicine, Division of Gastroenterology & Hepatology, 720 Rutland Ave, Ross 929, Baltimore, MD 21205. e-mail: jfoulke@jhmi.edu

ABBREVIATIONS

ATAC-seq (assay for transposase-accessible chromatin by sequencing), AUC (area under the curve), BMI (body mass index), DEG (differentially expressed gene), FDR (false discovery rate), FPKM (fragments per kilobase of transcript per million mapped reads), GOBP (Gene Ontology Biological

Process), ISC (intestinal stem cell), qRT-PCR (quantitative real-time polymerase chain reaction), ROC (receiver-operator curves), RYGB (roux-en-Y gastric bypass), TF (transcription factor), TSS (transcriptional start site)

ABSTRACT

Obesity is an epidemic with myriad health effects, but little is understood regarding individual obese phenotypes and how they may respond to therapy. Epigenetic changes associated with obesity have been detected in blood, liver, pancreas, and adipose tissues. Previous work using human organoids found that dietary glucose hyperabsorption is a steadfast trait in cultures derived from some obese subjects, but detailed transcriptional or epigenomic features of the intestinal epithelia associated with this persistent phenotype are unknown. This study evaluated differentially expressed genes and relative chromatin accessibility in intestinal organoids established from donors classified as non-obese, obese, or obese hyperabsorptive by body mass index and glucose transport assays. Transcriptomic analysis indicated that obese hyperabsorptive subject organoids have significantly upregulated dietary nutrient absorption transcripts and downregulated type I interferon targets. Chromatin accessibility and transcription factor footprinting predicted that enhanced HNF4G binding may promote the obese hyperabsorption phenotype. Quantitative RT-PCR assessment in organoids representing a larger subject cohort suggested that intestinal epithelial expression of CUBN, GIP, SLC5A11, and SLC2A5 were highly correlated with hyperabsorption. Thus, the obese hyperabsorption phenotype was characterized by transcriptional changes that support increased nutrient uptake by intestinal epithelia, potentially driven by differentially accessible chromatin. Recognizing unique intestinal phenotypes in obesity provides a new perspective in considering therapeutic targets and options to manage the disease.

Keywords: metabolic disease; intestinal organoids; ATAC-sequencing; intestinal nutrient absorption

INTRODUCTION

Obesity is a growing global public health crisis, with over 1.9 billion adults being overweight, and 650 million obese.(1) In 2016, the annual healthcare cost of adult obesity in the U.S. was $260.6 billion.(2)

55 The World Health Organization recognizes obesity as a risk factor for type 2 diabetes, coronary heart
56 disease, asthma, stroke, and multiple cancers. Obesity-associated diseases place an additional burden
57 on the healthcare system, with medical costs estimated to be 30% higher for obese individuals (BMI ≥30)
58 compared to those that are lean (BMI ≤25). Among the available therapies, bariatric surgery is the most
59 effective intervention for significant and sustained weight loss.(3) However, surgical outcomes are
60 heterogeneous with 15-35% of patients experiencing weight loss failure (<50% excess weight loss at 12-
61 18 months) after roux-en-Y gastric bypass (RYGB).(4, 5) Numerous hypotheses have fallen short of fully
62 identifying and characterizing molecular changes catalyzed by bariatric procedures.(6) Prediction of
63 individualized weight loss success based on phenotypic classification would be important to not only
64 guide selection of an effective intervention, but also to minimize potential risks and complications from
65 ineffective procedures.

66 Among the many phenotypes associated with obesity, accelerated intestinal glucose absorption
67 observed in nondiabetic obese subjects(7) is a striking example of an altered physiological response that
68 likely exacerbates the disease yet lacks full mechanistic understanding. Intestinal organoids/enteroids
69 are a unique experimental tool that stably retain intestinal region- and donor-specific genotype and
70 phenotypes.(8) In our prior study using patient-derived jejunal organoid monolayers from non-obese
71 (control group, G1) and obese subjects,(9) we found that a subset of obese donors exhibited significantly
72 increased epithelial glucose absorption capacity (obese hyperabsorption group, G2) relative to G1 non-
73 obese controls or other obese donor organoids (G3). This observation suggested that intestinal metabolic
74 phenotypes may be genetically encoded and differ among obese subjects. It further intimated that genetic
75 regulation of dietary sugar hyperabsorption may contribute to metabolic disease in G2 subjects.
76 Considering the relatively recent global surge in obesity development and the paucity of evidence for
77 specific protein-coding gene mutations to drive this outcome, we hypothesized that potential stable
78 epigenetic modifications in G2 individuals may account for the hyperabsorptive phenotype. In this study,
79 we analyzed the transcriptomes of differentiated organoid monolayers derived from 3 representative
80 donors for each group (G1, G2, and G3) to identify differentially expressed genes characteristic of each
81 group. We also conducted an assay for transposase-accessible chromatin sequencing (ATAC-seq) to

82 determine differential chromatin accessibility, and then carried out ATAC footprinting(10) and motif
83 analysis to detect putative transcription factors differentially occupying chromatin among the three
84 groups. Transcript levels distinctive for differing metabolic profiles were additionally validated in
85 differentiated organoid monolayers derived from an expanded cohort of non-obese and obese subjects.
86 Collectively, our data provides important insights into the dysregulated transcriptional state and altered
87 open chromatin landscape of intestinal epithelia in obese glucose hyperabsorptive subjects.
88

89 **RESULTS**

90 **Differential enrichment of metabolism-associated transcripts in obese donor-derived**
91 **differentiated organoid monolayers exhibiting glucose hyperabsorption**

92 Donor organoid lines were previously characterized as non-obese controls (G1, BMI ≤29.9, n=3),
93 obese with elevated intestinal glucose absorption relative to non-obese controls (G2, BMI ≥35, n=3), or
94 obese with intestinal glucose absorption similar to non-obese controls (G3, BMI ≥35, n=3) (**Table 1**).(9)
95 Bulk RNA-seq of differentiated organoid monolayers representing 3 donors in each group was conducted
96 to identify differentially expressed genes (DEG, absolute $\log_2$ fold change>2, p<0.05) (**Fig 1A** and
97 **Supplementary Table S1**). Principal component analysis demonstrated that the overall transcriptional
98 profiles among the three groups have considerable overlap, and that one individual in each group
99 appeared to segregate slightly from their respective group (**Fig 1B**). Comparison of G2 to either G1 or
100 G3 each revealed 456 DEGs, many of which function in dietary nutrient absorption, metabolism, and
101 regulation (**Fig 1C, D**). In contrast, G1 and G3 were distinguished by only 27 DEGs, suggesting highly
102 similar transcriptomes (**Fig 1E**). The enriched gene ontology biological processes (GOBP) in G2 included
103 glucose transport, cholesterol transport, and triglyceride homeostasis (Cluster #1, **Fig 1F, G**).
104 Downregulated GOBP in G2 epithelia included type I interferon signaling associated with regulation of
105 innate immune responses (Cluster #2, **Fig 1F, G**).

106 ***Sugar transport and metabolism.*** Significantly increased transcripts in G2 included the major
107 facilitators of intestinal glucose and fructose absorption: SLC2A2, SLC2A5, SLC5A1, and SLC5A4 (**Fig**
108 **1H**), which confirmed and expanded the findings of prior work.(9) As seen previously, levels of

109 gluconeogenic enzymes glucose-6-phosphatase (G6PC) and phosphoenolpyruvate carboxykinase
110 (PCK1) were also elevated. Ketohexokinase (KHK) and aldolase B (ALDOB) were also increased in G2,
111 suggesting that the epithelia is primed to catabolize an influx of dietary fructose entering through GLUT5.
112 Elevated transcripts for the brush border enzyme sucrase-isomaltase (SI) may enhance digestion of
113 sucrose and maltose into simple sugars for intestinal uptake, and dipeptidyl peptidase IV (DPP4) would
114 have potential to activate gut hormones involved in metabolic regulation.

115 ***Lipid transport and metabolism.*** Dietary fatty acids can be either passively absorbed or transit via
116 membrane-bound proteins. Transporters situated at the apical plasma membrane including fatty acid
117 translocase (CD36) and apolipoprotein M (APOM) were significantly upregulated in G2 (**Fig 1H**),
118 suggesting enhanced uptake ability. Additional fatty acid carriers included apolipoproteins APOA1,
119 APOA4, APOB, APOC2, and APOC3 that participate in lipid transport and act as enzyme cofactors for
120 lipid metabolism. Other amplified transcripts of note included receptors for lipoproteins (CUBN and
121 SCARB1), a channel for cholesterol-containing micelle import (NPC1L1), and SOAT2, which catalyzes
122 cholesterol esterification necessary for lipoprotein assembly. The rate limiting enzyme in mitochondrial
123 fatty acid oxidation (CPT1A) was relatively unchanged, suggesting that enterocytes are primarily
124 facilitating fatty acid transport rather than executing catabolism.

125 ***Bile acid absorption and signaling.*** Bile acids are normally introduced in the duodenum to assist
126 with solubilizing dietary fats and are subsequently reabsorbed in the distal ileum. Surprisingly, G2
127 demonstrated transcriptional enrichment in the jejunum for proteins involved in bile acid reabsorption that
128 are usually most prominent in distal ileum (**Fig 1H**). These included the major intracellular carrier for bile
129 acids, fatty acid binding protein 6 (FABP6), and the basolateral bile acid exporter subunits SLC51A and
130 SLC51B, as well as the bile acid responsive transcription factor FXR (NR1H4) and MALRD1, a cofactor
131 known to augment intestinal FGF19 secretion.[11] FGF19 transcripts were similar among the three groups,
132 which would be expected due to the absence of exogenous bile acids in the organoid culture media to
133 induce expression.

134 ***Intestinal hormones.*** Peptide hormones were another class of signaling molecule with differential
135 expression that distinguished G2 from G1 and G3. G2 subjects were found to overexpress guanylin

136 (GUCA2A), an intestinal peptide hormone produced by enterocytes and Paneth cells with pleiotropic
137 effects on epithelial transport via induction of cGMP synthesis (**Fig 1H**). Upregulated transcripts related
138 to enteroendocrine cell (EEC)-specific hormones, including glucose-dependent insulinotropic polypeptide
139 (GIP), motilin (MLN), somatostatin (SST), and the prohormone chromogranin A (CHGA) were also
140 detected. Given the relative rarity of EECs in organoids grown under conditions that do not optimize EEC
141 development,(12) the intrinsic emergence of these hormone transcripts is further evidence of differential
142 transcriptional controls in the G2 state.

143 Collectively, these results indicated that the obese glucose hyperabsorption phenotype (G2) is
144 characterized by upregulated transcription of nutrient transporters and metabolic regulators that may
145 contribute to dysregulated energy homeostasis in a subset of obese subjects.

146 **Downregulation of epithelial innate immune response transcripts in G2 and G3**

147 Many of the downregulated targets distinctive in G2 included interferon-stimulated genes (ISGs) and
148 downstream molecules linked to the type I interferon (IFN) signaling pathway (**Fig 1I**). These included
149 antiviral components such as interferon induced transmembrane proteins IFITM1, IFITM2, and IFITM3,
150 which restrict viral entry, and OAS2 and OASL, which act as sensors for double-stranded RNA. Innate
151 defense molecules including antimicrobial proteins REG1A, REG1B, REG3A, SLPI, and SEMG1 were
152 also significantly decreased relative to G1. Receptors with immune-associated functions including
153 IL18R1, LIFR, OSMR, CD40, and LTK were also reduced. Interestingly, G3 shared downregulation of
154 many innate immune-related genes that were observed in G2, implying that innate immune repression
155 may be shared among obese subjects regardless of their dietary nutrient absorption phenotype.

156 **Differential open chromatin regions in G2 suggest potential epigenetic alterations**

157 ATAC-seq was performed using the same differentiated organoid monolayer groups to investigate the
158 potential for an altered chromatin landscape that would account for the marked differential gene
159 expression in G2 relative to G1 or G3 (**Supplementary Table S2**). Comparison of G2 to G1 yielded 2,051
160 differential sites (**Fig 2A**), and G2 vs G3 indicated 3,549 differential sites (**Fig 2B**). G1 and G3 differed
161 by a more modest 491 sites (**Fig 2C**). The categorical locations of differential open chromatin were
162 similarly distributed in each of the three paired group comparisons. Notably, there were distinct open

163 chromatin regions proximal to transcriptional start sites (TSS) in G2 that were not equivalent in G1 nor
164 G3 (**Fig 2D**). Many of these sites coincided with increased levels of downstream gene transcripts,
165 suggesting an increase in enhancer activity.

166 When integrated with transcriptional data, pathways uniquely enriched in G2 were centered on
167 digestion and lipid transport/metabolism, an example of which is APOA4 (**Fig 2E**). In contrast, innate
168 immune-related transcripts appeared to be less prominent due to less open chromatin near the promoter
169 region of genes such as interferon-inducible antiviral enzyme 2'-5'-oligoadenylate synthetase 2 (OAS2)
170 (**Fig 2F**).

171 **ATAC footprinting indicates differential binding of transcription factors (TFs) associated with**
172 **metabolic and innate immune regulation in G2**

173 ATAC footprinting in G2 compared to G1 (**Fig 3A**) or G3 (**Fig 3B**) yielded significant differential binding
174 predictions that were in general agreement with transcriptional analyses and were highly similar between
175 the two comparators. Comparison of G1 and G3 did not render any significant differential binding results,
176 which further reflects their transcriptional similarity. G2 footprints suggested increased binding of nuclear
177 receptor ligand-activated TFs known to regulate digestive and metabolic processes, including hepatocyte
178 nuclear factor 4 paralogs (HNF4A, HNF4G) and numerous retinoic acid X receptor (RXR) heterodimers.
179 Lower scoring but significant binding prediction also implicated peroxisome proliferator activated
180 receptors (PPARA, PPARD, PPARG) which function as key regulators of lipid metabolism.

181 Integrated binding motif analysis ranked HNF4G as the top factor involved in G2 upregulated gene
182 transcription (p = 1e-40) (**Fig 3C**). HNF4G transcripts were also slightly upregulated ($\log_2$FC = 1.15) in
183 G2, suggesting that it may exert dominance in transcriptional regulation in the G2 state. Further, RNA-
184 seq FPKM values for HNF4A and HNF4G were approximately equivalent in G1 and G3, but HNF4G
185 FPKM was twice as high in G2 as in G1 or G3. A combination of increased open chromatin sites
186 conducive to HNF4 paralog binding and increased HNF4G levels suggest that the G2 state may be driven
187 at least in part by HNF4G activity.

188 Decreased footprinting was observed for Jun proto-oncogene (JUN), Fos proto-oncogene (FOS), and
189 activating transcription factor (ATF) family proteins that constitute the activator protein-1 (AP-1) TF

complex. AP-1 complexes regulate diverse cell responses related to inflammation, proliferation, differentiation, and apoptosis. Motif analysis ranked FOSL1 sites as least accessible in G2 compared to G1 (p = 1e-245) or to G3 (p = 1e-427). Although there were no significant differential footprints detected in G1 versus G3, motif analysis did indicate that FOSL2::JUN sites were less accessible in G3 (p = 1e-20), hinting that some AP-1 mediated processes may be attenuated in obese subjects with normative dietary nutrient absorption profiles. This was corroborated in the RNA-seq analysis showing that some of the innate immune-associated transcripts notably downregulated in G2 were also decreased in G3 relative to G1 (**Fig 1I**).

Analysis of differentiated organoid monolayers from additional subjects corroborates upregulated genes characteristic of G2

To follow up on the general findings from the nine selected donor organoids analyzed in RNA-seq and ATAC-seq experiments, we conducted glucose transport assays in differentiated organoid monolayers to identify additional G1 and G2 subjects (n=10 subjects/group, **Fig 4A**). This was followed by quantitative real-time PCR (qRT-PCR) analysis of cDNA isolated from differentiated monolayers. A panel of 10 genes related to dietary sugar/fat metabolism and gut hormones was chosen to validate transcriptional trends observed by RNA-seq. This expanded group of organoids did not identify any additional G3 donors. As expected, organoids that were phenotyped as G2 in glucose transport assays exhibited markedly increased transcript levels for the panel genes (presented quantitatively as ΔC_T values) relative to G1 donor organoids that were generally consistent with the RNA-seq findings (**Fig 4B, C**). Individual genes were compared among larger groups of G1 and G2 donor organoids using receiver-operator curves (ROC), and the calculated area under the curve (AUC) indicated that some transcripts (GIP, CUBN, SLC5A11, SLC2A5) appeared to have high predictive value (AUC≥0.910, p≤0.002), while other transcripts (GUCA2A, APOA4) were less robust indicators of group association (AUC≤0.780, p≤0.03) (**Fig 4D**).

DISCUSSION

Intestinal organoids derived from individuals with metabolic syndrome indicate that some subjects

217 have distinct transcriptional profiles consistent with dysregulated energy balance. The intestinal stem
218 cells of G2 subjects appeared to maintain genetic memory of their in vivo state with entrained upregulation
219 of fatty acid uptake, dietary sugar transport and metabolism, and specific gut hormones that was
220 independent of their immediate diet, given that all of the organoids were provided with the same
221 media/nutrition throughout the experimental process. Additionally, the transcriptional differences
222 observed were intrinsic to the epithelia and not dependent on other tissue components (mesenchyme,
223 immune, muscle, endothelia, lymphatics, neurons, or microbes). The transcriptional signatures appear
224 stable in organoid culture, as the cell lines tested were from a range of passages between 10-81 and
225 have been cryopreserved and rethawed multiple times.

226 Diet may play a major role in catalyzing the intestinal adaptation toward a hyperabsorptive phenotype.
227 Gut epithelia have the ability to undergo a rapid transcriptional shift toward increased fatty acid absorption
228 capacity in response to dietary nutrient influx, even observed within days of transitioning mice from
229 standard chow to a high fat diet.(13) Numerous studies have examined the influence of diet composition
230 on intestinal stem cell (ISC) behavior in animal models, finding that obesogenic high sugar and/or high
231 fat diets alter epithelial proliferation and lineage differentiation trajectories, and confirming that ISCs can
232 sense and respond to nutrients.(14-16) Studies evaluating the effect of diet on ISCs could also explain
233 the altered gut hormones evident in G2 subjects. Increased levels of GIP, SST, and MLN in G2 subjects
234 are consistent with observations that dietary exposures alter development of enteroendocrine cell
235 subtypes in mice.(13, 14) However, the duration and magnitude of dietary imbalance that may lead to
236 durable epigenetic modifications is not well defined. This study provides insight not only toward the
237 contribution of intestinal epithelia as a facilitator of excess nutrient absorption but also suggests that
238 acquisition of hard-wired transcriptional changes in these functions may undermine efforts to restrict
239 calorie intake.

240 TF footprinting and DNA binding motif analysis implicated HNF4 as the top-scoring regulator of the
241 G2 hyperabsorptive phenotype, and the role of HNF4 in intestinal absorptive/metabolic function is
242 strongly supported by prior animal studies. HNF4 has become known for orchestrating critical
243 programming of intestinal enterocyte maturation, brush border function, and fatty acid oxidation.(17-20)

244 HNF4A and HNF4G function as highly redundant paralogs in the intestinal epithelium, with HNF4G being
245 predominantly intestine-restricted.(21) Hnf4g$^{-/-}$ mice were protected from diet-induced obesity, likely due
246 to intestinal lipid malabsorption and increased GLP-1 levels.(22) Thus, the HNF4 paralogs and origin of
247 altered intestinal binding site accessibility in human obesity will be important targets for future study.
248 Increased occupancy of PPARD and retinoic acid X receptor α (RXRA) binding sites were also predicted
249 in G2, consistent with known roles in sensing and responding to diet. Despite evidence of more active
250 HNF4, PPARD, and RXRA, the transcripts for rate-limiting enzymes involved in fatty acid oxidation (FAO)
251 such as CPT1A were not upregulated. This could be a consequence of the limited fatty acid content in
252 standard organoid medium, so it would be interesting to assess whether FAO pathways are indeed
253 primed and would be more rapidly mobilized in G2 organoid monolayers than their G1 counterparts if
254 provided lipid-enriched media.

255 Downregulated transcripts in G2 were more difficult to functionally interpret as they group loosely with
256 various facets of innate immune responses. Footprinting and motif analysis suggest restricted binding of
257 AP-1 complex members which have pleiotropic cellular functions that include inflammation and immunity.
258 While intestinal epithelia are not first on the list of major immunity determinants, they do function as the
259 interface with microbial and environmental constituents by coordinating barrier function, luminal sampling
260 by professional immune cells, and secretion of defense molecules. A number of the downregulated genes
261 in G2 are interferon inducible and suggest blunting of type I IFN signaling. A correlation between obesity
262 and repressed type I IFN/antiviral responses has been noted in previous studies using human peripheral
263 blood mononuclear cells(23) and diet-induced obese mice.(24, 25) Thought to arise as a consequence
264 of chronic inflammation in metabolic disease, a dampened ability to mount IFN responses during obesity
265 may also be epigenetically controlled since the transcriptional phenotype persisted in organoid culture
266 and chromatin accessibility was restricted at associated TF binding sites. Interestingly, some degree of
267 overlap in the downregulated G2 and G3 transcripts relative to G1 hint that the innate immune changes
268 are not necessarily linked to the hyperabsorptive phenotype. Future work could evaluate interactions of
269 intestinal organoids in monolayer co-cultures with different immune cell populations to understand the
270 functional implications of the transcriptional profiles associated with each group.

271 To expand the number of study subjects and evaluate the prognostic potential of specific transcripts
272 as biomarkers, we conducted qRT-PCR in G1 and G2 differentiated organoid monolayers from 20
273 additional subjects and evaluated the AUC of ΔC_T values plotted as receiver-operator curves (ROC). Our
274 sample size (n=10 subjects/group) of G1 and G2 demonstrated statistically significant sensitivity and
275 specificity for 9 of the 10 markers measured. This implies that the G2 phenotype has potential to be
276 characterized through transcriptomic evaluation of intestinal epithelial biopsies in lieu of time- and labor-
277 intensive functional organoid-based assays, and that with further cohort expansion and validation, the
278 development of a qRT-PCR-based diagnostic panel may be feasible.

279 Organoid cultures also provided evidence that obesity phenotypes are complex and that mechanisms
280 other than intestinal sugar hyperabsorption may contribute to disease. Thus, some obese subject
281 organoids (G3) lacked evidence of altered intestinal absorption and metabolic dysregulation. Profiles of
282 additional donor organoids will be necessary to define the proportion of obese patients with intestinal
283 hyperabsorption, and to understand how this phenotype impacts the severity of their metabolic disease,
284 comorbidities, and potential response to therapeutic intervention. However, this study and prior work(9)
285 highlight the importance of personalized approaches to characterizing metabolic disease phenotypes. It
286 is not surprising that the intestinal epithelium undergoes profound imprinted alterations in the obesogenic
287 state given that prior studies have detected differential DNA methylation patterns in other tissues (blood,
288 liver, pancreas, adipocytes) during obesity in humans(26-28) and in rodents on high-fat diet.(26, 29-32)
289 Future studies to understand drivers of the epigenetic changes and identify strategies to limit or reverse
290 intestinal hyperabsorption in these patients could transform clinical approaches to obesity management.

291

292 **METHODS**

293 **Human organoid cultures**

294 Organoid cultures were established from adult jejunal tissue obtained during upper endoscopy
295 procedures or tissue discarded following bariatric surgeries as described previously.(9) Informed consent
296 from study participants was obtained under protocols approved by the Institutional Review Boards at
297 Johns Hopkins University (NA_0038329), Baylor College of Medicine (H-31793 and H-31910), and Mayo

298 Clinic Florida (22-001407). All experiments were performed in accordance with review board guidelines
299 and regulations. Recruited subjects were ≥18 years of age, and tissue samples were de-identified such
300 that only age, sex, and BMI were recorded. Glucose absorption phenotype was determined using
301 differentiated organoid monolayers incubated with 25 mM glucose buffer in the apical compartment for 2
302 h. Organoids classified as Group 1 were established from non-obese donors (BMI ≤ 29.9 kg/m2) and
303 exhibited low intestinal epithelial glucose absorption (≤125 μM glucose detected in basolateral buffer).
304 Organoids in Group 2 were from obese donors (BMI ≥ 35 kg/m2) and showed elevated intestinal epithelial
305 glucose absorption (>125 μM glucose in basolateral buffer). Organoids in Group 3 were from obese
306 donors (BMI ≥ 35 kg/m2) with glucose absorption profiles that were similar to non-obese donors. BMI
307 classification was based on World Health Organization guidelines. Information regarding patient
308 characteristics (age, sex, BMI, glucose absorption phenotype) is provided in **Table 1**. Organoids were
309 cultured in Expansion Media (EM), as previously described (Advanced Dulbecco's Modified Eagle
310 Medium/Ham's F-12, 10 mM HEPES, 0.2 mM GlutaMAX, 50% v/v Wnt3A-conditioned media, 15% v/v R-
311 spondin-1-conditioned media, 10% v/v of Noggin-conditioned media, 50 ng/ml human epidermal growth
312 factor (EGF), 500 nM A83-01, 10 μM SB 202190, 1× B27 supplement, 1 mM N-acetylcysteine).(33, 34)
313 At the time of culture initiation and each weekly culture passage, EM was supplemented with 10 μM
314 CHIR99021 and 10 μM Y-27632 for the first 48 h. Growth factor conditioned media was obtained from
315 cell lines expressing Wnt3A (murine L-Wnt3A, CRL-2647, American Type Culture Collection), R-spondin-
316 1 (human HA-Rspo1-Fc/HEK293, kindly provided by Dr. Calvin Kuo, Stanford University, USA), and
317 Noggin (murine Noggin-Fc/HEK293).(35) EM was refreshed every 2-3 d, and organoids were passaged
318 every 7 days. Passage numbers used in this study ranged from 10 to 81.

319 **Organoid monolayers**

320 Organoid monolayers were prepared as previously described.[36, 37] Briefly, isolated organoid fragments
321 resuspended in EM were plated on 24-well plate permeable tissue culture inserts (Corning Transwell
322 3470; 0.4 μm pore, 0.33 cm^2 surface area) coated with collagen IV (10 μg/cm^2, Sigma C5533). To monitor
323 progress toward confluence, transepithelial electrical resistance (TER) was measured using an EVOM2
324 voltohmmeter (World Precision Instruments). Monolayers judged to be confluent by TER measurement

325 (>300 $\Omega \cdot cm^2$) and inspection by light microscopy were transferred to differentiation media (DM;
326 Expansion Media lacking Wnt3A, R-spondin-1, A83-01, and SB 202190). Monolayers were used for
327 experiments 5 days after transfer to DM. For the sequencing experiments, differentiated organoid
328 monolayers were digested with Accutase (MilliporeSigma) at 25 °C for 20 min or until cells exhibited
329 rounding and dissociation by light microscopy. The cell suspension was transferred to a low-binding
330 microcentrifuge tube (USA Scientific) and washed with Sorting Buffer (PBS, 25 mM HEPES pH 7.4, 0.5%
331 bovine serum albumin, 5 mM EDTA). Cells were pelleted at 500 xg, 4 °C, 5 min. Buffer was aspirated
332 and cell pellets were snap frozen in liquid nitrogen for RNA-seq, or resuspended at 75,000 cells/100 µL
333 Anti-Freezing Buffer (Advanced DMEM/F-12, 10% fetal calf serum, 10% DMSO) for ATAC-seq, and
334 immediately stored at -80 °C until processed for the respective sequencing applications.

335 **Glucose transport**

336 Transport of D-glucose was measured in a procedure similar to that described previously.(9) Differentiated
337 organoid monolayers on Transwell inserts were confirmed to be confluent by TER measurements prior to
338 initiating the experiment. Monolayers were washed once (100 µL upper/apical chamber, 600 µL
339 lower/basolateral chamber) with mannose buffer (50 mM HEPES pH 7.4, 138 mM NaCl, 4.7 mM KCl, 1.25
340 mM $MgSO_4$, 1.25 mM $CaCl_2$, 0.5% bovine serum albumin, 5 mM mannose) and then incubated in mannose
341 buffer at 37 °C, 5% CO_2, 30 min. An aliquot (200 µL) was removed from the lower chamber (time 0
342 measurement) and replaced with an equivalent volume of fresh mannose buffer. The mannose buffer in the
343 upper chamber was aspirated, replaced with 100 µL of 25 mM glucose buffer (50 mM HEPES pH 7.4, 128 mM
344 NaCl, 4.7 mM KCl, 1.25 mM $MgSO_4$, 1.25 mM $CaCl_2$, 0.5% bovine serum albumin, 25 mM D-glucose), and
345 then returned to the incubator for 2 h. TER was re-measured after 2 h to confirm that the monolayers remained
346 intact during the incubation, and 200 µL of buffer in the lower chamber was sampled. The glucose
347 concentration in the buffers was measured using an Amplex Red Glucose Assay kit (ThermoFisher Scientific).
348 The final 96-well plate absorbance was read at 570 nm on an AccuSkan microplate reader (ThermoFisher
349 Scientific).

350 **RNA sequencing**

351 The organoid lines used for RNA-seq and ATAC-seq were previously characterized for glucose
352 absorption phenotype.(9) Total RNA was isolated from cells and purified by DNase I treatment using the

353 RNeasy Micro kit (Qiagen). RNA-seq libraries were prepared by Illumina TruSeq RNA Library Preparation
354 Kit v2 and sequenced on the Illumina HiSeq 4000 platform in the Mayo Clinic Medical Genomics Core.
355 Mayo RNA-sequencing (MAP-RSeq) analysis pipeline was used to perform gene expression analysis.
356 FASTQ readings (paired end; 100 bp) were aligned to hs38 with TopHat2, generating raw gene and exon
357 counts using featureCount, and sample quality was determined by RSeQC. EdgeRv3.8.6 was used for
358 differential expression analysis and to compare groups. Genes with an absolute $\log_2$ fold change
359 ($\log_2$FC) >1.5 and false discovery rate (FDR) <0.05 were considered to be significantly differentially
360 expressed.

361 **ATAC sequencing**

362 Approximately 50,000 nuclei isolated from organoid monolayers were utilized for ATAC-seq. The
363 transposition reaction was carried out in a thermomixer at 37° C for 30 minutes and oscillated at 1,000
364 rpm. The size of the library DNA was determined by a Fragment Analyzer from the amplified and purified
365 library. The ATAC-seq library was amplified by PCR. By targeting known highly accessible and closed
366 chromatin sites with real-time PCR, the enrichment of each library's accessible regions was determined
367 and expressed as a fold difference. BWA was used to map paired end reads to the hs38 genome. Picard
368 SortSam was used to convert SAM files into BAM files and sort by chromosomal coordinates. Picard
369 MarkDuplicates was used to remove PCR duplicates. Processed BAM files were used to call the peak
370 by MACS2. BAM files and peak files obtained from MACS2 was processed using DiffBind to identify
371 differentially accessible genomic loci. Using an FDR threshold of 0.05, Homer was used to annotate the
372 differentially accessible loci to the closest transcription start site (TSS). GREAT was used to conduct gene
373 ontology on the genome regions determined in the ATAC-seq analysis with default settings. Motif analysis
374 was completed by the findMotifsGenome.pl command in Homer. Transcription factor footprinting analysis
375 was conducted using the TOBIAS computational framework.(10)

376 **Quantitative real-time PCR (qRT-PCR)**

377 Organoid lines used for qRT-PCR were newly collected for this study. Total RNA was extracted from
378 differentiated organoid monolayers using the PureLink RNA Mini Kit (Invitrogen) and reverse transcribed
379 to complementary DNA using SuperScript VILO Master Mix (Invitrogen). Reactions for qRT-PCR were

380 carried out in triplicate using 5 ng cDNA, gene-targeted oligonucleotide pairs (sequences in **Table 2**), and
381 Power SYBR Green Master Mix (Invitrogen) on a QuantStudio 12K Flex instrument (Applied Biosystems).
382 For each organoid line, the gene target was normalized to the average C_T for 18S ribosomal RNA
383 (RN18S) and GAPDH to obtain ΔC_T values. Statistical significance was calculated by unpaired student's
384 t-test. Receiver-operator curves (ROC) plotting the true positive rate (sensitivity) versus the false positive
385 rate (1 – specificity), and the associated area under the curve and *p*-values for each target, were prepared
386 using GraphPad Prism 10 using 95% confidence intervals and the Wilson/Brown method.

387

388 **DATA AVAILABILITY**

389 Data is provided within the manuscript and in supplementary tables. The complete RNA-seq and ATAC-
390 seq datasets generated and analyzed in the current study are available online in the Gene Expression
391 Omnibus (accession number pending).

392

393 **REFERENCES**

394 1. **Congdon P, and Amugsi D**. Editorial: The obesity epidemic: Causes, context, prevention. *Front*
395 *Public Health* 10: 1030180, 2022.

396 2. **Cawley J, Biener A, Meyerhoefer C, Ding Y, Zvenyach T, Smolarz BG, and Ramasamy A**. Direct
397 medical costs of obesity in the United States and the most populous states. *J Manag Care Spec Pharm*
398 27: 354-366, 2021.

399 3. **Maciejewski ML, Arterburn DE, Van Scoyoc L, Smith VA, Yancy WS, Jr., Weidenbacher HJ,**
400 **Livingston EH, and Olsen MK**. Bariatric Surgery and Long-term Durability of Weight Loss. *JAMA Surg*
401 151: 1046-1055, 2016.

402 4. **Christou NV, Look D, and Maclean LD**. Weight gain after short- and long-limb gastric bypass in
403 patients followed for longer than 10 years. *Ann Surg* 244: 734-740, 2006.

404 5. **Higa K, Ho T, Tercero F, Yunus T, and Boone KB**. Laparoscopic Roux-en-Y gastric bypass: 10-
405 year follow-up. *Surg Obes Relat Dis* 7: 516-525, 2011.

406 6. **Kohli R, Stefater MA, and Inge TH**. Molecular insights from bariatric surgery. *Rev Endocr Metab*

407 *Disord* 12: 211-217, 2011.

408 7. **Nguyen NQ, Debreceni TL, Bambrick JE, Chia B, Wishart J, Deane AM, Rayner CK, Horowitz**
409 **M, and Young RL**. Accelerated intestinal glucose absorption in morbidly obese humans: relationship to
410 glucose transporters, incretin hormones, and glycemia. *J Clin Endocrinol Metab* 100: 968-976, 2015.

411 8. **Gunther C, Winner B, Neurath MF, and Stappenbeck TS**. Organoids in gastrointestinal diseases:
412 from experimental models to clinical translation. *Gut* 71: 1892-1908, 2022.

413 9. **Hasan NM, Johnson KF, Yin J, Baetz NW, Fayad L, Sherman V, Blutt SE, Estes MK, Kumbhari**
414 **V, Zachos NC, and Kovbasnjuk O**. Intestinal stem cell-derived enteroids from morbidly obese patients
415 preserve obesity-related phenotypes: Elevated glucose absorption and gluconeogenesis. *Mol Metab* 44:
416 101129, 2021.

417 10. **Bentsen M, Goymann P, Schultheis H, Klee K, Petrova A, Wiegandt R, Fust A, Preussner J,**
418 **Kuenne C, Braun T, Kim J, and Looso M**. ATAC-seq footprinting unravels kinetics of transcription factor
419 binding during zygotic genome activation. *Nat Commun* 11: 4267, 2020.

420 11. **Wang LX, Frey MR, and Kohli R**. The Role of FGF19 and MALRD1 in Enterohepatic Bile Acid
421 Signaling. *Front Endocrinol (Lausanne)* 12: 799648, 2021.

422 12. **Zeve D, Stas E, de Sousa Casal J, Mannam P, Qi W, Yin X, Dubois S, Shah MS, Syverson EP,**
423 **Hafner S, Karp JM, Carlone DL, Ordovas-Montanes J, and Breault DT**. Robust differentiation of
424 human enteroendocrine cells from intestinal stem cells. *Nat Commun* 13: 261, 2022.

425 13. **Enriquez JR, McCauley HA, Zhang KX, Sanchez JG, Kalin GT, Lang RA, and Wells JM**. A dietary
426 change to a high-fat diet initiates a rapid adaptation of the intestine. *Cell Rep* 41: 111641, 2022.

427 14. **Aliluev A, Tritschler S, Sterr M, Oppenlander L, Hinterdobler J, Greisle T, Irmler M, Beckers J,**
428 **Sun N, Walch A, Stemmer K, Kindt A, Krumsiek J, Tschop MH, Luecken MD, Theis FJ, Lickert H,**
429 **and Bottcher A**. Diet-induced alteration of intestinal stem cell function underlies obesity and prediabetes
430 in mice. *Nat Metab* 3: 1202-1216, 2021.

431 15. **Lickwar CR, Davison JM, Kelly C, Mercado GP, Wen J, Davis BR, Tillman MC, Semova I,**
432 **Andres SF, Vale G, McDonald JG, and Rawls JF**. Transcriptional Integration of Distinct Microbial and
433 Nutritional Signals by the Small Intestinal Epithelium. *Cell Mol Gastroenterol Hepatol* 14: 465-493, 2022.

434 16. **Alonso S, and Yilmaz OH**. Nutritional Regulation of Intestinal Stem Cells. *Annu Rev Nutr* 38: 273-
435 301, 2018.
436 17. **Babeu JP, Darsigny M, Lussier CR, and Boudreau F**. Hepatocyte nuclear factor 4alpha
437 contributes to an intestinal epithelial phenotype in vitro and plays a partial role in mouse intestinal
438 epithelium differentiation. *Am J Physiol Gastrointest Liver Physiol* 297: G124-134, 2009.
439 18. **Boyd M, Bressendorff S, Møller J, Olsen J, and Troelsen JT**. Mapping of HNF4alpha target genes
440 in intestinal epithelial cells. *BMC Gastroenterol* 9: 68, 2009.
441 19. **Chen L, Toke NH, Luo S, Vasoya RP, Aita R, Parthasarathy A, Tsai YH, Spence JR, and Verzi**
442 **MP**. HNF4 factors control chromatin accessibility and are redundantly required for maturation of the fetal
443 intestine. *Development* 146: 2019.
444 20. **Chen L, Vasoya RP, Toke NH, Parthasarathy A, Luo S, Chiles E, Flores J, Gao N, Bonder EM,**
445 **Su X, and Verzi MP**. HNF4 Regulates Fatty Acid Oxidation and Is Required for Renewal of Intestinal
446 Stem Cells in Mice. *Gastroenterology* 158: 985-999 e989, 2020.
447 21. **Chen L, Toke NH, Luo S, Vasoya RP, Fullem RL, Parthasarathy A, Perekatt AO, and Verzi MP**.
448 A reinforcing HNF4-SMAD4 feed-forward module stabilizes enterocyte identity. *Nat Genet* 51: 777-785,
449 2019.
450 22. **Ayari S, Gil-Iturbe E, le Gléau L, Osinski C, Kapel N, Soula HA, Leturque A, Andreelli F, Clément**
451 **K, Serradas P, and Ribeiro A**. Hnf4g invalidation prevents diet-induced obesity via intestinal lipid
452 malabsorption. *Journal of Endocrinology* 252: 31-44, 2022.
453 23. **Teran-Cabanillas E, Montalvo-Corral M, Caire-Juvera G, Moya-Camarena SY, and Hernandez**
454 **J**. Decreased interferon-alpha and interferon-beta production in obesity and expression of suppressor of
455 cytokine signaling. *Nutrition* 29: 207-212, 2013.
456 24. **Smith AG, Sheridan PA, Harp JB, and Beck MA**. Diet-induced obese mice have increased
457 mortality and altered immune responses when infected with influenza virus. *J Nutr* 137: 1236-1243, 2007.
458 25. **Gaur P, Riehn M, Zha L, Koster M, Hauser H, and Wirth D**. Defective interferon amplification and
459 impaired host responses against influenza virus in obese mice. *Obesity (Silver Spring)* 29: 1272-1278,
460 2021.

461 26. **Multhaup ML, Seldin MM, Jaffe AE, Lei X, Kirchner H, Mondal P, Li Y, Rodriguez V, Drong A,**
462 **Hussain M, Lindgren C, McCarthy M, Näslund E, Zierath JR, Wong GW, and Feinberg AP**. Mouse-
463 human experimental epigenetic analysis unmasks dietary targets and genetic liability for diabetic
464 phenotypes. *Cell Metab* 21: 138-149, 2015.
465 27. **McAllan L, Baranasic D, Villicaña S, Brown S, Zhang W, Lehne B, Adamo M, Jenkinson A,**
466 **Elkalaawy M, Mohammadi B, Hashemi M, Fernandes N, Lambie N, Williams R, Christiansen C,**
467 **Yang Y, Zudina L, Lagou V, Tan S, Castillo-Fernandez J, King JWD, Soong R, Elliott P, Scott J,**
468 **Prokopenko I, Cebola I, Loh M, Lenhard B, Batterham RL, Bell JT, Chambers JC, Kooner JS, and**
469 **Scott WR**. Integrative genomic analyses in adipocytes implicate DNA methylation in human obesity and
470 diabetes. *Nature Communications* 14: 2784, 2023.
471 28. **Samblas M, Milagro FI, and Martínez A**. DNA methylation markers in obesity, metabolic syndrome,
472 and weight loss. *Epigenetics* 14: 421-444, 2019.
473 29. **Widiker S, Karst S, Wagener A, and Brockmann GA**. High-fat diet leads to a decreased
474 methylation of the Mc4r gene in the obese BFMI and the lean B6 mouse lines. *J Appl Genet* 51: 193-197,
475 2010.
476 30. **Milagro FI, Campión J, García-Díaz DF, Goyenechea E, Paternain L, and Martínez JA**. High fat
477 diet-induced obesity modifies the methylation pattern of leptin promoter in rats. *Journal of Physiology and*
478 *Biochemistry* 65: 1-9, 2009.
479 31. **Keleher MR, Zaidi R, Hicks L, Shah S, Xing X, Li D, Wang T, and Cheverud JM**. A high-fat diet
480 alters genome-wide DNA methylation and gene expression in SM/J mice. *BMC Genomics* 19: 888, 2018.
481 32. **Zhang P, Chu T, Dedousis N, Mantell BS, Sipula I, Li L, Bunce KD, Shaw PA, Katz LS, Zhu J,**
482 **Argmann C, O'Doherty RM, Peters DG, and Scott DK**. DNA methylation alters transcriptional rates of
483 differentially expressed genes and contributes to pathophysiology in mice fed a high fat diet. *Molecular*
484 *Metabolism* 6: 327-339, 2017.
485 33. **Foulke-Abel J, In J, Yin J, Zachos NC, Kovbasnjuk O, Estes MK, de Jonge H, and Donowitz M**.
486 Human Enteroids as a Model of Upper Small Intestinal Ion Transport Physiology and Pathophysiology.
487 *Gastroenterology* 150: 638-649 e638, 2016.

488 34. **Sato T, Stange DE, Ferrante M, Vries RG, Van Es JH, Van den Brink S, Van Houdt WJ, Pronk**
489 **A, Van Gorp J, Siersema PD, and Clevers H**. Long-term expansion of epithelial organoids from human
490 colon, adenoma, adenocarcinoma, and Barrett's epithelium. *Gastroenterology* 141: 1762-1772, 2011.
491 35. **Heijmans J, van Lidth de Jeude JF, Koo BK, Rosekrans SL, Wielenga MC, van de Wetering M,**
492 **Ferrante M, Lee AS, Onderwater JJ, Paton JC, Paton AW, Mommaas AM, Kodach LL, Hardwick JC,**
493 **Hommes DW, Clevers H, Muncan V, and van den Brink GR**. ER stress causes rapid loss of intestinal
494 epithelial stemness through activation of the unfolded protein response. *Cell Rep* 3: 1128-1139, 2013.
495 36. **In J, Foulke-Abel J, Zachos NC, Hansen AM, Kaper JB, Bernstein HD, Halushka M, Blutt S,**
496 **Estes MK, Donowitz M, and Kovbasnjuk O**. Enterohemorrhagic Escherichia coli reduce mucus and
497 intermicrovillar bridges in human stem cell-derived colonoids. *Cell Mol Gastroenterol Hepatol* 2: 48-62
498 e43, 2016.
499 37. **In JG, Foulke-Abel J, Clarke E, and Kovbasnjuk O**. Human Colonoid Monolayers to Study
500 Interactions Between Pathogens, Commensals, and Host Intestinal Epithelium. *J Vis Exp* 2019.
501

502 **ACKNOWLEDGEMENTS**

503 The authors thank Dr. Mary K. Estes (Baylor College of Medicine) for sharing four jejunal organoid lines
504 (J2, J4, J11, and J12) used in this study. Tissue culture facilities were provided by the Johns Hopkins
505 Digestive Diseases Basic & Translational Research Core Center (National Institutes of Health P30
506 DK089502). RNA-seq was performed by the Genome Analysis Core, Mayo Clinic Rochester. ATAC-seq
507 was conducted by the Epigenomics Development Laboratory, Center for Cell Signaling in
508 Gastroenterology, Mayo Clinic Rochester (National Institutes of Health P30 DK084567). Sequence
509 assembly pipelines, differential gene expression, and ATAC footprinting were carried out by the
510 Bioinformatics Core, Mayo Clinic Rochester. Quantitative PCR was conducted on instrumentation
511 provided by the Johns Hopkins Genetic Resources Core Facility.
512

513 **GRANTS**

This study was supported Mayo Clinic intramural funds (to D.S.B. and V.K.), and Johns Hopkins Division of Gastroenterology & Hepatology intramural funds and National Institutes of Health grant K01 DK113043 (to J.F.A.).

DISCLOSURES

No conflicts of interest, financial or otherwise, are declared by the authors.

DISCLAIMERS

Dr. Kovbasnjuk is an employee of the National Institutes of Health, USA. The content of this manuscript is solely the responsibility of the author and does not necessarily represent the official views of the National Institutes of Health, USA.

AUTHOR CONTRIBUTIONS

D.S.B., O.K., V.K., and J.F.A. conceived and designed research; D.S.B., Z.L., J.H.L., T.M., A.V.B., R.L., A.D., and J.F.A. performed experiments; D.S.B., Z.L., J.H.L., T.M., A.V.B., T.O., O.K., and J.F.A. interpreted results of experiments; Z.L., T.M., A.V.B, and J.F.A. prepared figures; D.S.B, Z.L., T.O., O.K., and J.F.A. drafted and edited manuscript; all authors approved final version of the manuscript.

TABLES

Table 1. Organoid donor characteristics. Deidentified subject designator (organoid line), group classification (G1, non-obese; G2, obese hyperabsorptive; G3, obese) based on glucose transport phenotype, demographic information (age, sex), body mass index (BMI), and passage number for each organoid line studied. n.r., not recorded; n.a., not applicable.

Group	Organoid Line	Originating Institution	Absorption Phenotype	Age	Sex	BMI	Organoid passage used in RNA-based experiments	Patient ID previously reported(9)
G1	J1	Johns Hopkins	low	n.r.	F	≤25	P38	3
G1	J11	Baylor	low	n.r.	F	23	P29	4
G1	J23	Johns Hopkins	low	46	F	21	P11	5
G2	J2	Baylor	high	52	F	≥35	P81	7

G2	J4	Baylor	high	n.r.	F	≥35	P33	8
G2	J21	Johns Hopkins	high	42	F	43	P10	9
G3	J12	Baylor	low	n.r.	M	≥35	P28	13
G3	J17	Johns Hopkins	low	49	F	53	P15	16
G3	J20	Johns Hopkins	low	48	F	51	P13	14
G1	1	Johns Hopkins	low	81	F	22.8	P16	n.a.
G1	23	Johns Hopkins	low	57	M	23	P9	n.a.
G1	24	Johns Hopkins	low	63	F	28	P7	n.a.
G1	25	Johns Hopkins	low	63	M	28.2	P8	n.a.
G1	26	Johns Hopkins	low	65	F	24	P6	n.a.
G1	27	Johns Hopkins	low	73	F	23.8	P4	n.a.
G1	28	Johns Hopkins	low	67	F	27.1	P5	n.a.
G1	0020	Mayo	low	20	M	23.1	P12	n.a.
G1	0021	Mayo	low	21	F	22.1	P10	n.a.
G1	0022	Mayo	low	37	M	19.5	P10	n.a.
G2	0003	Mayo	high	51	F	32.7	P7	n.a.
G2	0004	Mayo	high	58	M	36.3	P5	n.a.
G2	0005	Mayo	high	73	F	36.3	P8	n.a.
G2	0009	Mayo	high	73	F	36.7	P6	n.a.
G2	0012	Mayo	high	55	F	34.3	P4	n.a.
G2	0013	Mayo	high	32	F	42.7	P6	n.a.
G2	0014	Mayo	high	47	F	36.9	P7	n.a.
G2	0015	Mayo	high	46	F	43.5	P4	n.a.
G2	0018	Mayo	high	71	F	38.3	P3	n.a.
G2	0031	Mayo	high	55	F	32.1	P4	n.a.

Table 2. Oligonucleotide sequences. Oligonucleotides used in qRT-PCR assays.

Gene Symbol	Accession Number	Forward primer (5'-3')	Reverse primer (5'-3')
18S rRNA	NR_003286	GTAACCCGTTGAACCCCATT	CCATCCAATCGGTAGTAGCG
GAPDH	NM_002046	AGGGCTGCTTTTAACTCTGGT	CCCCACTTGATTTTGGAGGGA
APOA4	NM_000482	CAGTGTGGCAAGAAACTCCT	GTAGTCCCACATCACCGTG
CD36	NM_001001548	TGTCCTGGCTGTGTTTGG	TGTCTGTAAACTTCTGTGCCTG
CUBN	NM_001081	TCTCAGCAATCCAAATCAGGG	ACCACAAAGTCTCCACATCAG
G6PC	NM_000151	AGGGAAAGATAAAGCCGACC	AGCAAGGTAGATTCGTGACAG
GIP	NM_004123	GCCAGTCAAGCTAATAGGAAGG	AGAGGTTTGTCTGATCCAGC
GUCA2A	NM_033553	ATGAATGCCTTCCTGCTCTC	CCTGGAGGTCTTTGAGCTTC
KHK	NM_006488	ACTCCAATGGCAACCGTAC	ACCTTCTCAAAGTCTGTAGCAG
SLC2A2	NM_000340	TGCTGTCTCTGTATTCCTTGTG	TGCTCACATAACTCATCCAAGAG
SLC2A5	NM_003039	CCGTGTCCATGTTTCCATTTG	ATCCCATTAAGATCGCAGGC
SLC5A11	NM_052944	CTGTACTTCCTCTTTGTCCTGG	GTCCACTTCCAACATTGCTG

540 **FIGURE LEGENDS**

541 **Figure 1. Differential gene expression among the organoid donor groups.** (**A**) Experimental design
542 and donor phenotypes of groups 1, 2, and 3. (**B**) Principal component analysis (PCA) of the nine donors
543 following RNA-seq analysis. Colors distinguish donors in each of the three groups. (**C**) Volcano plot
544 depicting significantly upregulated (red) or downregulated (blue) transcripts ($\log_2$FC > |2|, $p < 0.05$) in
545 paired comparisons of G2/G1, (**D**) G2/G3, and (**E**) G1/G3. (**F**) Heatmap of relative expression for
546 significant DEGs in G2 compared to G1 or G3. Cluster 1 contains DEG that were significantly upregulated
547 in G2, and Cluster 2 contains DEG that were significantly downregulated in G2. Z scores for each gene
548 were computed from $\log_2$(FPKM+1) contained in the respective clusters. (**G**) Gene ontology (GO) terms
549 representing major biological processes characteristic of Clusters 1 and 2. (**H**) Heatmap ($\log_2$FC) for
550 selected transcripts distinctively upregulated in G2 that are associated with dietary sugar
551 transport/metabolism, fat absorption/transport, bile acid absorption, and gut hormones. (**I**) Heatmap of
552 selected transcripts distinctively downregulated in G2 that loosely group as factors involved in innate
553 immune functions.

554

555 **Figure 2. Differential open chromatin regions among the organoid donor groups.** (**A**) Differential
556 open chromatin regions ($\log_2$FC > |2|, $p < 0.05$) identified from ATAC-seq in G1 vs G2, (**B**) G2 vs G3, and
557 (**C**) G1 vs G3. (**D**) Heatmaps of differential open chromatin proximal to transcription start sites (TSS,
558 within 2 kb upstream or downstream) for each donor. (**E**) Summed ATAC-seq peak tracks for each of the
559 three groups representing the upstream and protein coding region for APOA4, which had increased
560 accessibility in G2. (**F**) Summed peak tracks for OAS2, which had decreased accessibility in G2 relative
561 to the other groups.

562

563 **Figure 3. Differential transcription factor binding events inferred from ATAC footprinting.** (**A**)
564 Volcano plot of differential binding scores in G1 vs G2 and (**B**) G2 vs G3. There were no significant
565 differential binding events in G1 vs G3. (**C**) Top three most and least accessible TF motifs in G2 when
566 compared to G1, ranked by *p*-value.

567

568 **Figure 4. Validation of differentially expressed intestinal epithelial biomarkers in obese**
569 **hyperabsorptive subjects. (A)** Glucose transport measured as the D-glucose concentration
570 accumulated in the lower Transwell chamber (basolateral buffer) after 2 h feeding with buffer containing
571 25 mM D-glucose. Organoids were established from non-obese or obese subjects (n=10 organoids in
572 each group). Each dot represents an independent transport experiment and is the average of two
573 Transwell technical replicates. *, $p \leq 0.05$; **, $p \leq 0.01$; ***, $p \leq 0.001$. Absorption phenotype/group
574 assignment was determined using a cutoff of 125 μM D-glucose (dotted line). Organoids were unique
575 from those analyzed by next-generation sequencing and the prior Hasan et al study. (**B**) Transcripts
576 measured by quantitative real-time PCR (qRT-PCR) expressed as ΔC_T, the difference between the target
577 gene C_T and the average of the C_T for housekeeping transcripts RN18S and GAPDH. (**C**) Heatmap of
578 ΔC_T values depicted in panel B to illustrate individual donor organoid ΔC_T trends. Increasing intensity of
579 the red color indicates a smaller ΔC_T value (higher transcript levels). (**D**) Receiver-operator curves (ROC)
580 for each biomarker analyzed by qRT-PCR. Each graph includes the respective area under the curve
581 (AUC) and *p*-value.

582

Figure 1.

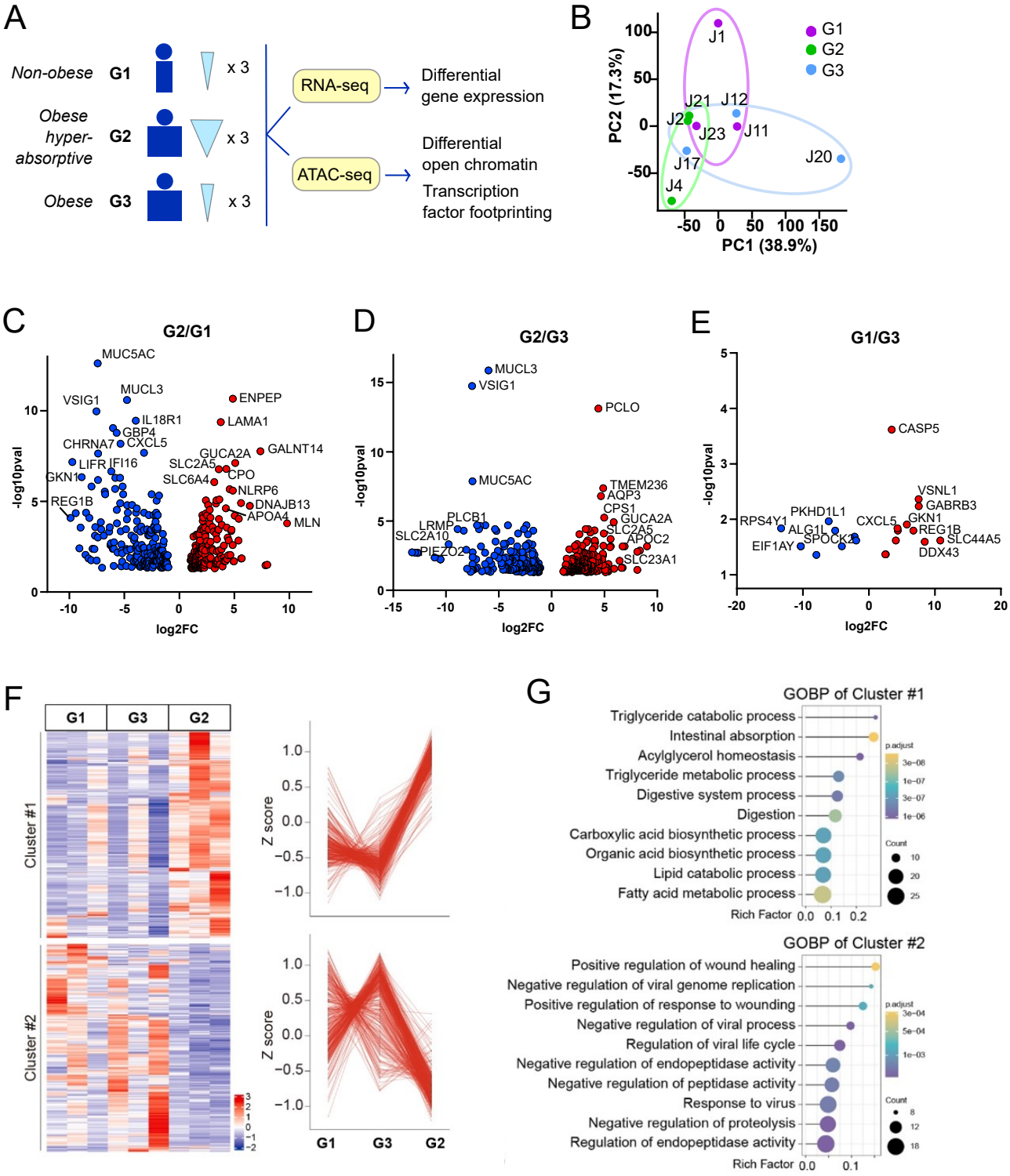
A
Non-obese G1
Obese hyper-absorptive G2
Obese G3
x 3
x 3
x 3
RNA-seq
ATAC-seq
Differential gene expression
Differential open chromatin
Transcription factor footprinting
B
G1
G2
G3
PC2 (17.3%)
PC1 (38.9%)
J1
J21
J12
J2
J23
J11
J17
J20
J4
C
G2/G1
-log10pval
log2FC
MUC5AC
MUCL3
VSIG1
ENPEP
IL18R1
LAMA1
GBP4
CHRNA7
CXCL5
GALNT14
LIFR
IFI16
GUCA2A
SLC2A5
GKN1
CPO
SLC6A4
NLRP6
REG1B
DNAJB13
APOA4
MLN
D
G2/G3
-log10pval
log2FC
MUCL3
VSIG1
PCLO
MUC5AC
TMEM236
AQP3
CPS1
PLCB1
GUCA2A
LRMP
SLC2A5
SLC2A10
APOC2
PIEZO2
SLC23A1
E
G1/G3
-log10pval
log2FC
CASP5
VSNL1
GABRB3
PKHD1L1
RPS4Y1
CXCL5
GKN1
ALG1L
REG1B
SPOCK2
SLC44A5
EIF1AY
DDX43
F
G1
G3
G2
Cluster #1
Cluster #2
Z score
G1
G3
G2
G
GOBP of Cluster #1
Triglyceride catabolic process
Intestinal absorption
Acylglycerol homeostasis
Triglyceride metabolic process
Digestive system process
Digestion
Carboxylic acid biosynthetic process
Organic acid biosynthetic process
Lipid catabolic process
Fatty acid metabolic process
Rich Factor
p.adjust
Count
GOBP of Cluster #2
Positive regulation of wound healing
Negative regulation of viral genome replication
Positive regulation of response to wounding
Negative regulation of viral process
Regulation of viral life cycle
Negative regulation of endopeptidase activity
Negative regulation of peptidase activity
Response to virus
Negative regulation of proteolysis
Regulation of endopeptidase activity
Rich Factor
p.adjust
Count

Figure 1 (continued)

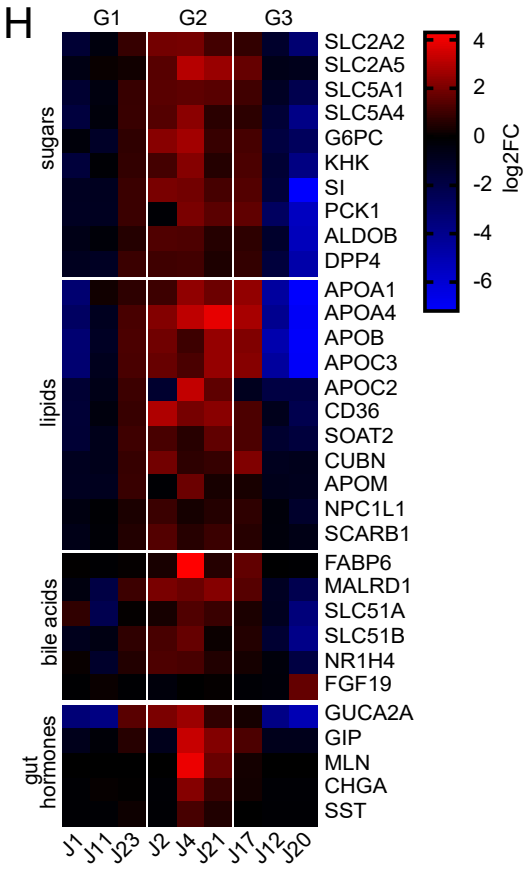

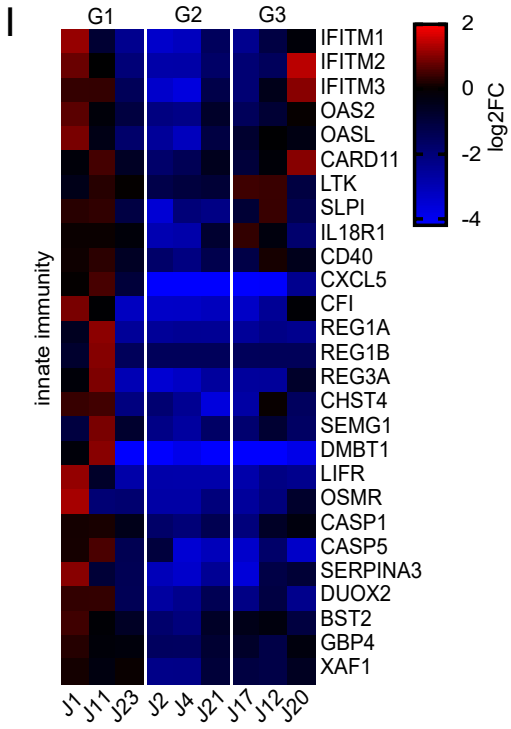

Figure 2.

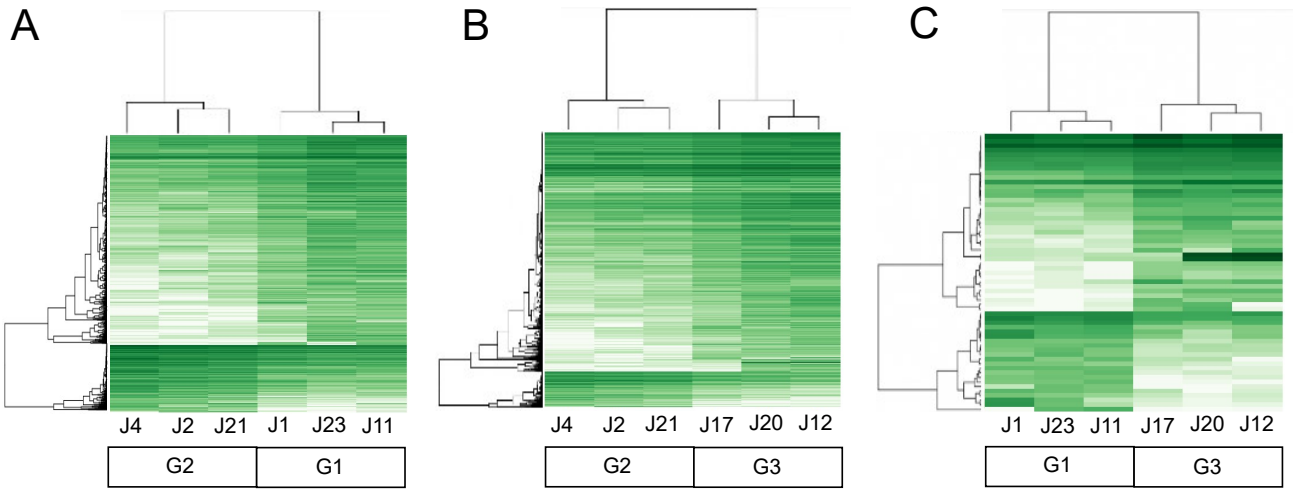
A
J4 J2 J21 J1 J23 J11
G2 G1
B
J4 J2 J21 J17 J20 J12
G2 G3
C
J1 J23 J11 J17 J20 J12
G1 G3

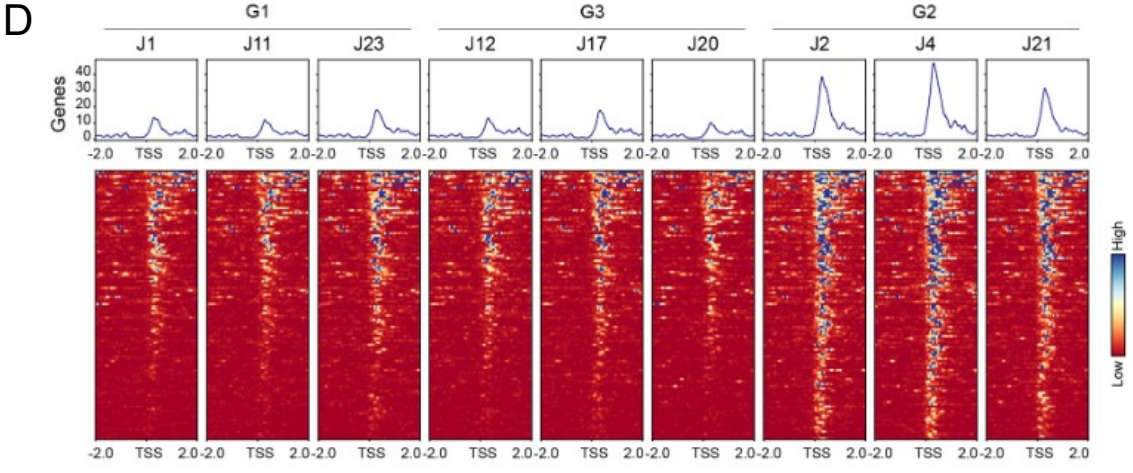
D
G1
J1 J11 J23
G3
J12 J17 J20
G2
J2 J4 J21
Genes
40 30 20 10 0
-2.0 TSS 2.0
High
Low

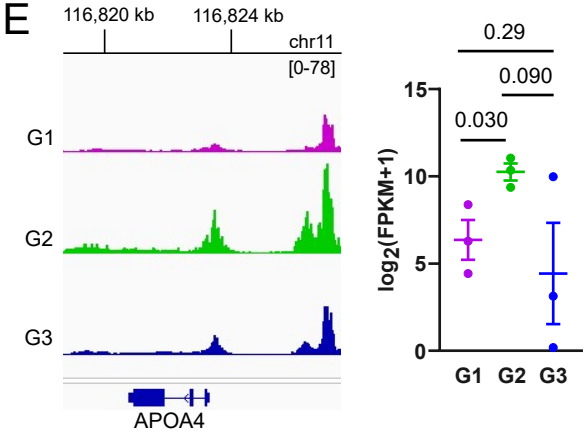
E
116,820 kb
116,824 kb
chr11
[0-78]
G1
G2
G3
APOA4
0.29
0.090
0.030
15
10
5
0
log2(FPKM+1)
G1 G2 G3

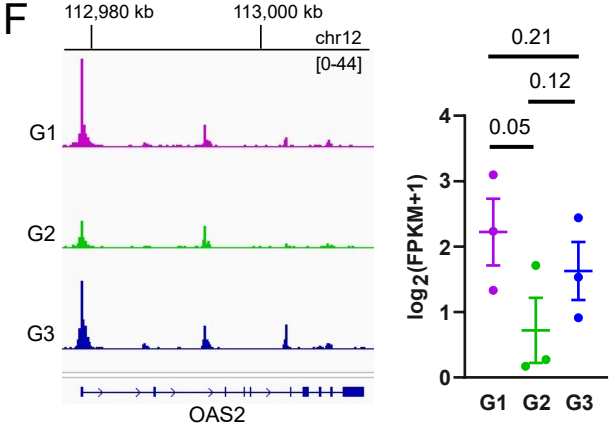
F
112,980 kb
113,000 kb
chr12
[0-44]
G1
G2
G3
OAS2
0.21
0.12
0.05
4
3
2
1
0
log2(FPKM+1)
G1 G2 G3

Figure 3.

A

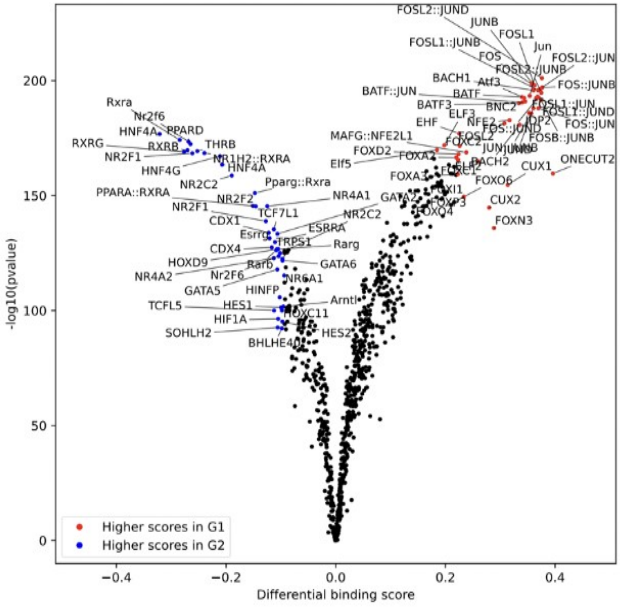

B

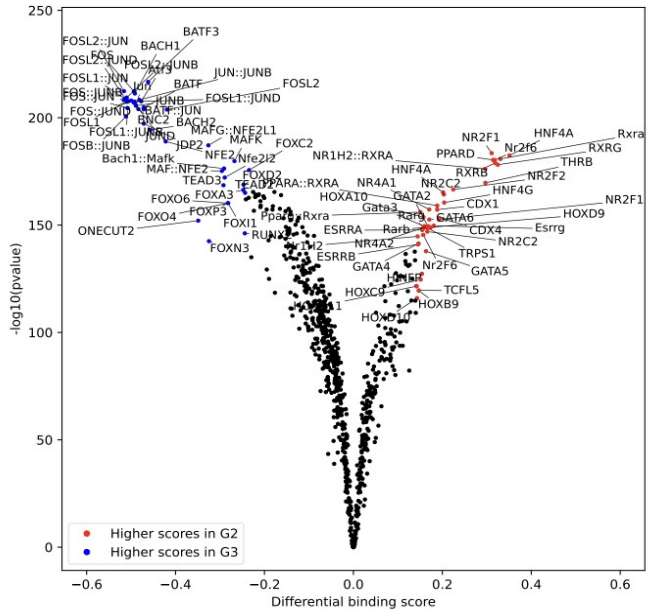

C

Enriched/more accessible in G2

G2 motif	P value
HNF4G	1e-40
CDX2	1e-24
DLX5	1e-14

Less accessible in G2

G1 motif	P value
FOSL1	1e-245
ELF3	1e-108
FOXM1	1e-84

Figure 4.

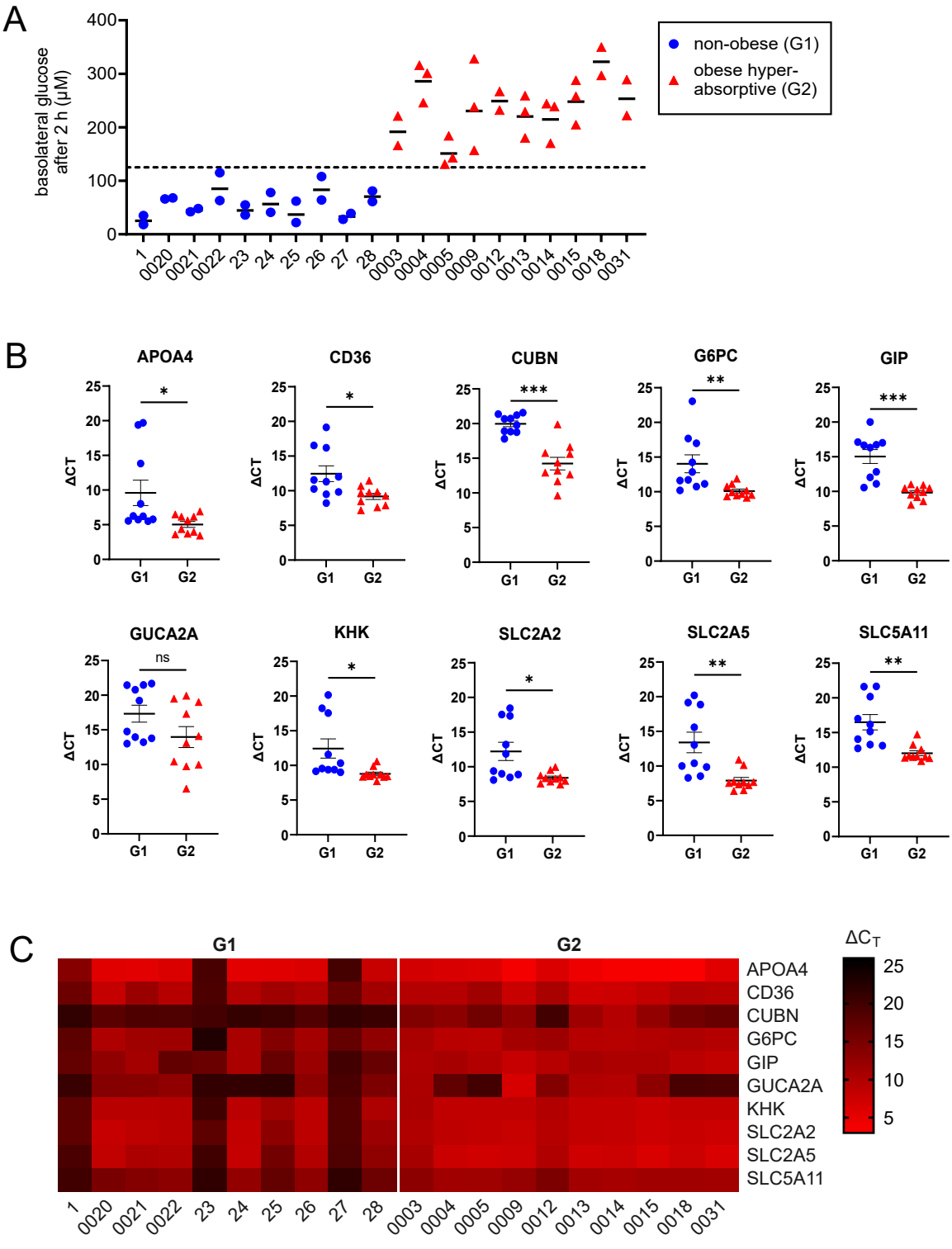
A
basolateral glucose after 2 h (µM)
400
300
200
100
0
1
0020
0021
0022
23
24
25
26
27
28
0003
0004
0005
0009
0012
0013
0014
0015
0018
0031
non-obese (G1)
obese hyper-absorptive (G2)
B
APOA4
CD36
CUBN
G6PC
GIP
GUCA2A
KHK
SLC2A2
SLC2A5
SLC5A11
ΔCT
G1
G2
*
**
***
ns
C
G1
G2
APOA4
CD36
CUBN
G6PC
GIP
GUCA2A
KHK
SLC2A2
SLC2A5
SLC5A11
ΔC_T
25
20
15
10
5

Figure 4 (continued)
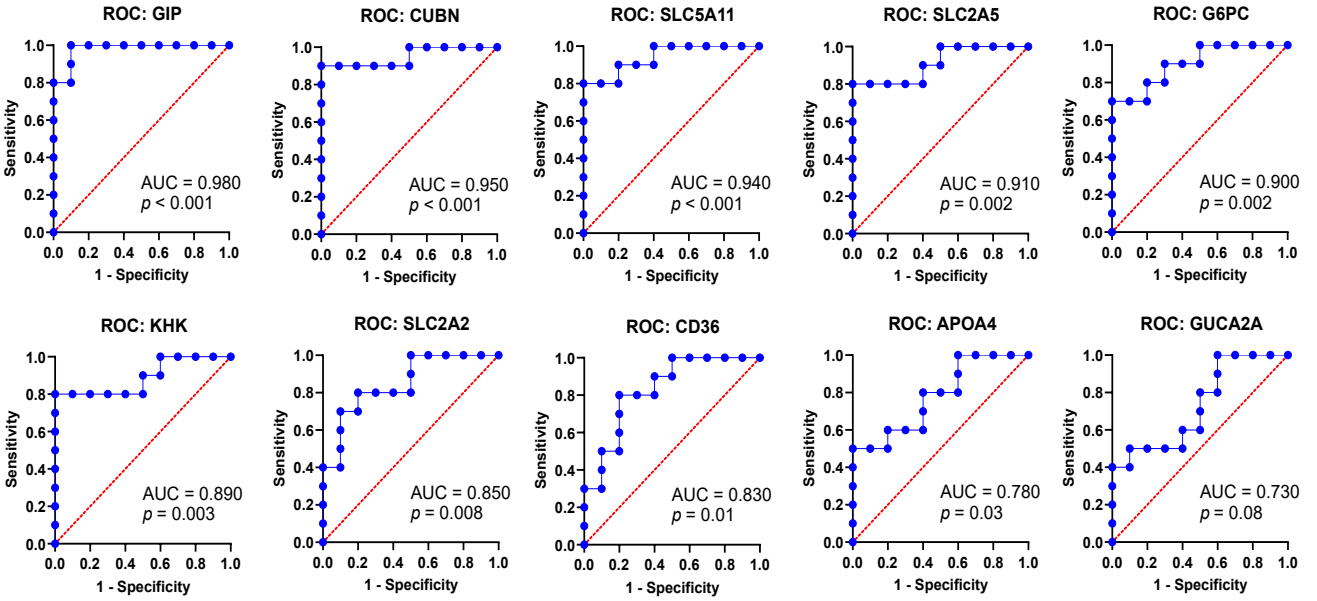
D